CHAPTER V

Reduced graphene oxide (rGO)/PEDOT:PSS/Nickel oxide (NiO) ternary nanocomposite as anode catalyst for methanol oxidation

5.1 Introduction

Catalyst materials with unique morphologies, which can increase cycling stability and electrocatalytic activity of methanol oxidation in direct methanol fuel cell along with environment friendliness, have been in active research. The excellent electrocatalytic activity owing to the existence of oxidation state along with thermal and chemical stability makes the transition metal oxides suitable material for electrocatalytic applications [1-4]. The characteristics of bulk semiconducting transition metal oxides have been significantly transformed in nanoscale transition metal oxides due to quantum confined effects, high surface area, and defect induced. These significant properties of nanoscale semiconducting metal oxides make them a promising candidate for the design of nanodevices such as efficient catalyst in energy storage and conversion systems, and in the development of sensitive sensors. Among the various metal oxides, nickel oxide (NiO) attains significant attention in the field of electrochemical systems such as supercapacitors, electrochromic films, water splitting, electrochemical sensors, Li-ion batteries and methanol oxidation [5-10]. The stable structure, electrochemical activeness, good electrical conductivity and rich redox chemistry are the significant properties of NiO [11, 12]. Recently, NiO nanostructures have been used as electrocatalyst including nanofibers [13], nanorods [14], nanoparticles [15, 16], nanoflakes [17], nanoplates [18] and hollow spheres [19, 20]. Nanostructured NiO can offer superior electrical conductivity and cycle performance by compositing with highly conducting carbon based materials [21-23]. According to prior art [24], mesoporous NiO samples possess large numbers of both nanoplates and nanorods at certain reaction conditions and exhibit a Tafel slope of 62 mV dec^{-1} and achieved a current density of 41.6 mA cm^{-2} at 1.6 V (vs. RHE). 2D reduced graphene oxide (rGO), a derivative of graphene, can be a promising material for preparation of composites owing to its significant surface area, very high electrical conductivity, considerable chemical stability and good resistance toward

Baruah, B., Biswas, R. and Deb, P., *International Journal of Energy Research,* 46(12):16394-16415, 2022.

corrosion. rGO can increase the rate of transport of electrons and ions and also the stability of redox active materials. The film forming capability, strong mechanical strength and environment friendliness of the conducting polymer (CP), Poly(3,4-ethylenedioxythiophene):poly(styrene-sulfonate) (PEDOT:PSS) make it a useful material for electrode preparation.

Engineering at the surface and interface of electrocatalyst by forming composite is one of the effective routes to enhance intrinsic activity of the catalyst. The strong electronic interactions between two or more than two active materials in heterostructure may result in reconstructed active sites [25]. Therefore, higher activity can be obtained at the reconstructed active sites than that of individual materials. Thus chemisorption process over the catalyst surface is facilitated. For example, NiNPs-R/PPy/CPE exhibits larger ethanol electrooxidation current density and stability as compared to platinum and non-regenerated NiNPs/PPy/CPE electrodes [26]. In another study, a higher methanol oxidation activity and good catalytic stability is observed at Ni/NiO/MWCNT composites modified GCE, where the composite has been synthesized by combustion method [27]. A functional metal oxide CeO_2 has been used to modify a spinel oxide $CoFe_2O_4$ for improvement of electrocatalytic activity [28]. The CeO_2@$CoFe_2O_4$/NF hybrid nanostructure exhibits superior urea oxidation reaction and oxygen evolution reaction activities which can be attributed to availability of large number of more electroactive sites and a fast electron transport [28].

In present work, rGO/PEDOT:PSS/NiO nanocomposite has been explored for its potential application as an electrocatalyst in methanol oxidation reaction. The two dimensional (2D) NiO nanoplates provide large surface area with remarkable electroactive sites for adsorption of methanol molecules and excellent electron transport properties. Among the adjacent one dimensional (1D) nanostructures, there are plenty of open pores which can boost the accessibility of chemical along with mass transportation of electrolytes deep into the electrodes [29]. Thus, 1D nanostructure offers easy path for electronic and ionic transport and hence decreases the electrical resistance. Moreover, the interface between the two different nanostructures may reveal new properties that are different from either of the single nanostructures. 2D nanoplates have large number of electroactive sites at the surface conjugation with 1D nanorods providing additional active sites for electrocatalysis.

5.2 Morphological characterizations

5.2.1 Scanning electron microscopy

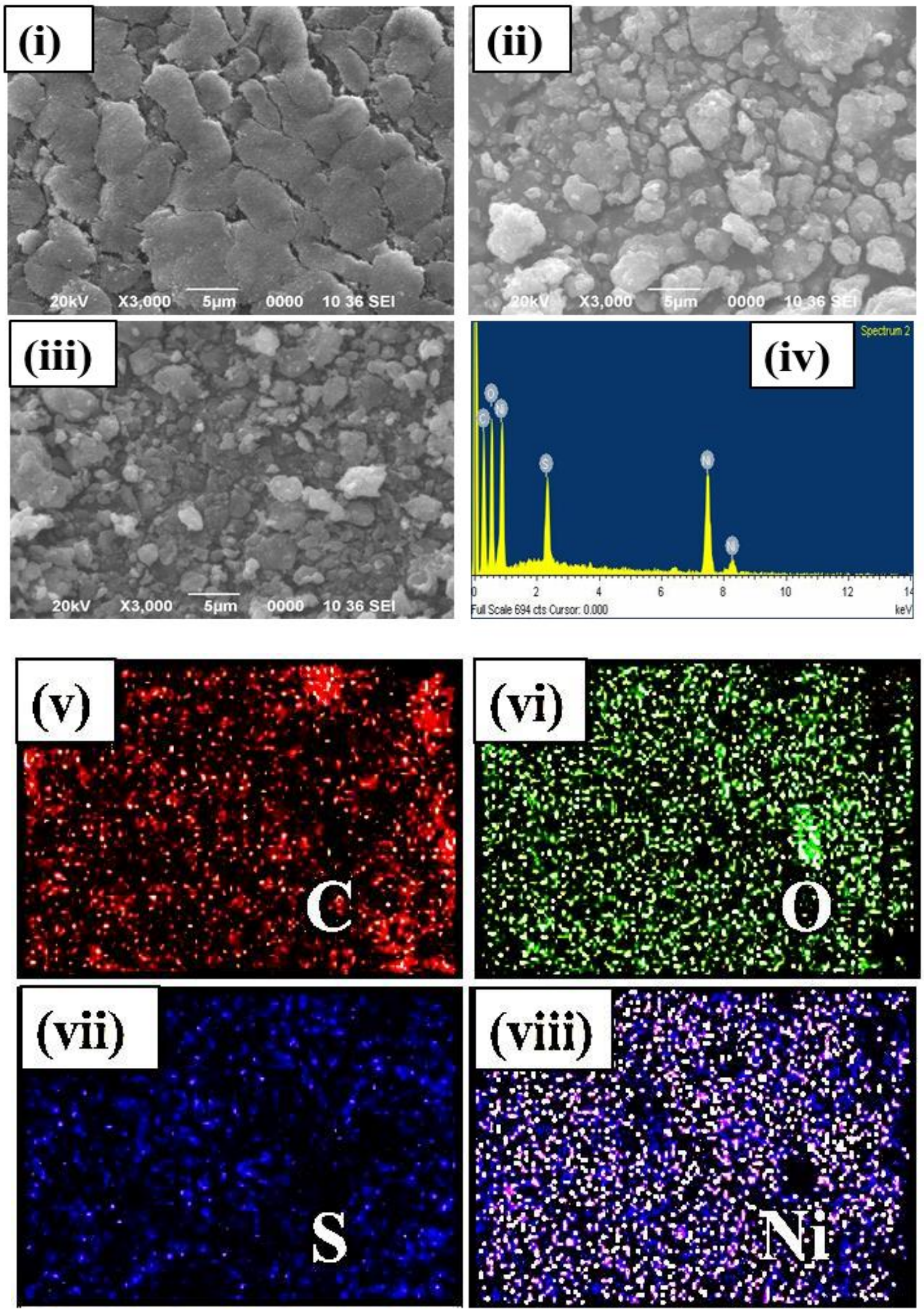

Figure 5.1: *SEM images of (i) NiO, (ii) PEDOT:PSS/NiO and (iii) rGO/PEDOT:PSS/NiO nanocomposites. (iv) EDX spectrum of rGO/PEDOT:PSS/NiO nanocomposite. The elemental mapping of the elements (v) C, (vi) O, (vii) S and (viii) Ni in rGO/PEDOT:PSS/NiO nanocomposite.*

The morphologies of the catalysts have been depicted in Figures 5.1 (i)-(iii). The SEM image of pure NiO shows plate like structure (Figure 5.1 (i)), whereas formation of clusters has been observed in SEM image (Figure 5.1 (ii)) of PEDOT:PSS/NiO nanocomposite. Figure 5.1 (iii) reveals porous surface of rGO/PEDOT:PSS/NiO nanocomposite, where plate-like structure of NiO has no longer been observed. Energy dispersive X-ray spectroscopy has been done to identify the elements present in rGO/PEDOT:PSS/NiO nanocomposite as presented in Figure 5.1 (iv). The atomic percentages of C, O, S and Ni are 58.12%, 32.95%, 2.07% and 6.86% respectively. The percentage of oxygen is higher in comparison to nickel due to the presence of oxygen in PEDOT:PSS. The carbon signals come from the polymer and rGO. Small percentage of sulfur is also present in the nanocomposite due to PEDOT:PSS. Apart from these elements, no peaks from other elements are seen in the spectrum, suggesting purity of the nanocomposite. The energy dispersive X-ray elemental mapping has been performed to investigate the element distribution of rGO/PEDOT:PSS/NiO nanocomposite as depicted in Figures 5.1(v)-(viii). The elemental mapping shows the uniform distribution of C, O, S and Ni in rGO/PEDOT:PSS/NiO nanocomposite.

5.2.2 Transmission electron microscopy

Figure 5.2 (i) depicts the TEM image of sheet-like graphene with crumple structure. The TEM images of pure NiO demonstrate the coexistence of nanorods (length 42 to 60 nm and diameter 5-8 nm) and nanoplates (24-38 nm in width) as illustrated in Figures 5.2 (ii) and (iii). Ostwald ripening is the reason behind the large size of nanoplates and nanorods, where smaller nanostructures dissolute and form larger nanostructures due to high solubility and surface energy within the solution. The TEM images of PEDOT:PSS/NiO (Figures 5.2 (iv) and (v)) ensure well dispersion of NiO nanorods and nanoplates in PEDOT:PSS matrix. Figures 5.2 (vi) and (vii) show that in rGO/PEDOT:PSS/NiO nanocomposite, PEDOT:PSS coated NiO nanorods and nanoplates are embedded inside rGO nanosheets.

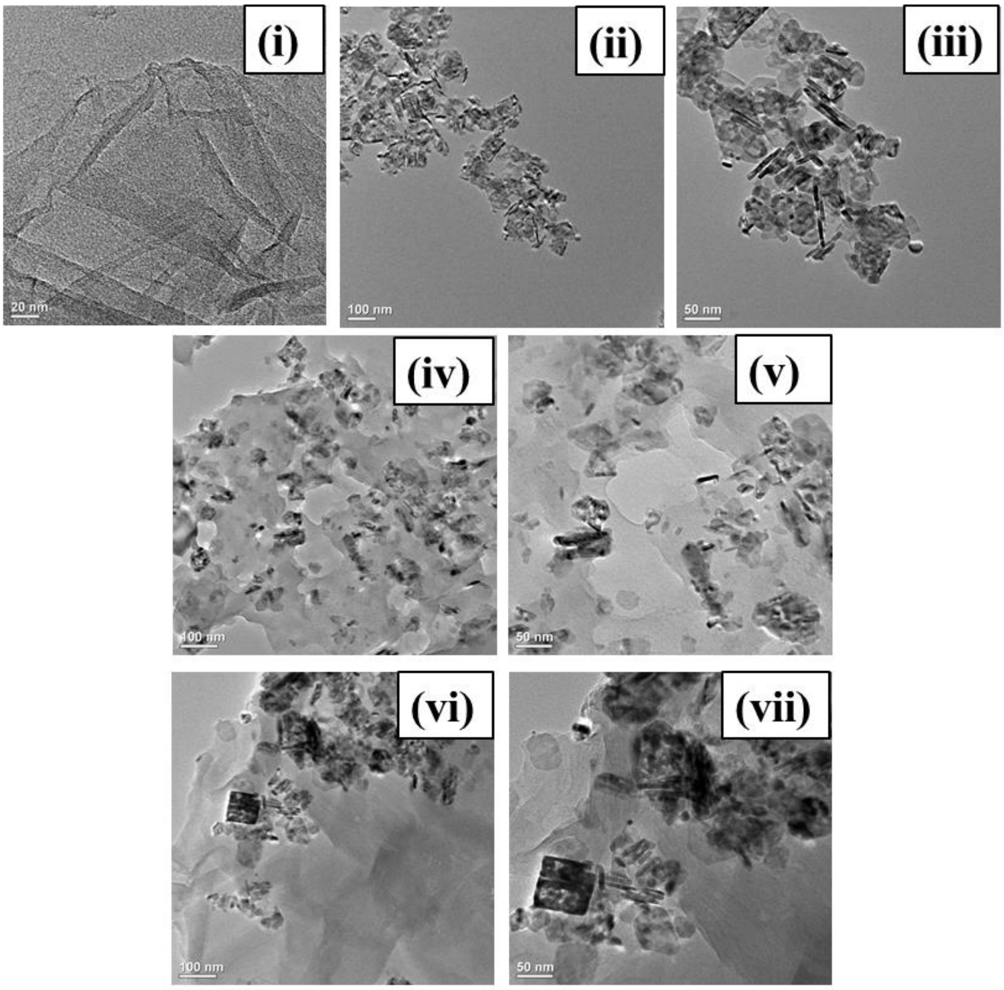

Figure 5.2: *TEM images of (i) rGO nanosheet, (ii) and (iii) NiO, (iv) and (v) PEDOT:PSS/NiO nanocomposite, (vi) and (vii) rGO/PEDOT:PSS/NiO nanocomposite.*

5.3 Physical Characterizations

5.3.1 X-ray diffraction

The structural investigation of the samples has been carried out using XRD and results are presented in Figure 5.3. As shown in Figure 5.3 (i), GO reveals a sharp XRD peak at 11.8^o assigned to (002) plane having interlayer distance of 0.74 nm. This peak shifts to 25.2^o in rGO and the interlayer distance becomes 0.35 nm as presented in Figure 5.3 (i)). Another small intense peak is seen at 43° corresponding to (100) plane due to turbostratic disorder present in carbon materials [30]. The characteristic XRD peaks in PEDOT:PSS (Figure 5.3 (i)) are seen at 17.7^o and 26.2^o, attributing to the interlayer distance of 5 and 3.4 Å, respectively. The small intense peak of PEDOT:PSS at 17.7^o appears due to amorphous PSS chain structure and the broad peak at 26.2^o arises owing to π-π interchain stacking between (010) planes [31]. In Figure 5.3 (ii), well-defined XRD peaks of NiO are observed at 35.3°, 41.5° and 61°, signifying (111), (200) and (220) planes of NiO crystals, respectively. PEDOT:PSS/NiO nanocomposite exhibits a broad peak around 24° (Figure 5.3 (ii)) assigned to (010) plane indicating the amorphous nature of PEDOT:PSS. Moreover a broad hump is observed around 24° in the diffraction pattern of rGO/PEDOT:PSS/NiO nanocomposite due to presence of rGO in Figure 5.3 (ii).

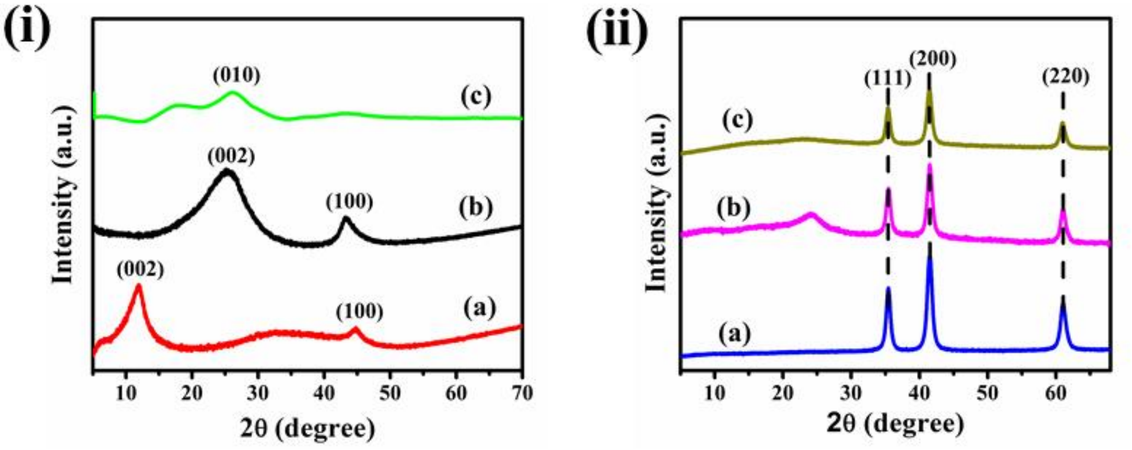

Figure 5.3: *(i) XRD patterns of (a) GO, (b) rGO and (c) PEDOT:PSS; (ii) XRD patterns of (a) NiO, (b) PEDOT:PSS/NiO nanocomposite and (c) rGO/PEDOT:PSS/NiO ternary nanocomposite.*

5.3.2 Raman spectroscopy

Figure 5.4 (i) depicts the Raman spectrum of NiO. The characteristic bands of NiO appear at 494 and 1043 cm^{-1} corresponding to first-order longitudinal optical (LO) one-phonon (1p) mode of NiO and second order phonon modes (2p) of 2LO, respectively [32]. In Figure 5.4 (ii), the Raman bands of PEDOT:PSS at 570 and 986 cm^{-1} correspond to C-S-C ring deformation and C-C alkyl anti-symmetrical stretching vibration mode, respectively. The bands at 1245 and 1356 cm^{-1} arise due to C_α-C_α inter ring stretching and C_β-C_β stretching deformations, respectively. The sharp Raman band at 1432 cm^{-1} is assigned to C_α=C_β (C_α is the adjacent to sulphur atom, while C_β is adjacent to C_α) symmetrical stretching, while the bands at 1503 and 1560 cm^{-1} are attributed to C_α=C_β antisymmetric stretching and quinoid structure, respectively [33]. However, a small intense band around 2876 cm^{-1} arises owing to the existence of C-H stretching vibration [31]. The dominant Raman bands of rGO, D band at 1345 cm^{-1} represents breathing modes of carbon ring or K-point phonons of A_{1g} symmetry that associated with defects present in carbon structures and G band at 1581 cm^{-1} is attributed to in plane stretching vibration caused by E_{2g} phonon mode of sp^2 bonded C atoms. 2D band at 2706 cm^{-1} is assigned as the second order of D band, which is related to the number of layers present in rGO sheets [34]. The broad 2D band in comparison to G band suggests the presence of multilayer rGO sheets. The blue shift of G band in rGO by 12 cm^{-1} after incorporation of PEDOT:PSS and NiO indicates intermolecular interaction among rGO, PEDOT:PSS and NiO. Incorporation of rGO in PEDOT:PSS/NiO nanocomposite induces change in the conformation of PEDOT from benzoid to quinoid structure due to significant amount of interaction between PEDOT:PSS and basal plane of rGO nanosheets. In rGO/PEDOT:PSS/NiO nanocomposite, the major peaks of rGO i.e. D, G and 2D bands are prominent while the bands of PEDOT:PSS and NiO are vanished. This is due to the existence of π-π interactions between rGO and PEDOT:PSS and transformation of coil to chain structure of PEDOT:PSS.

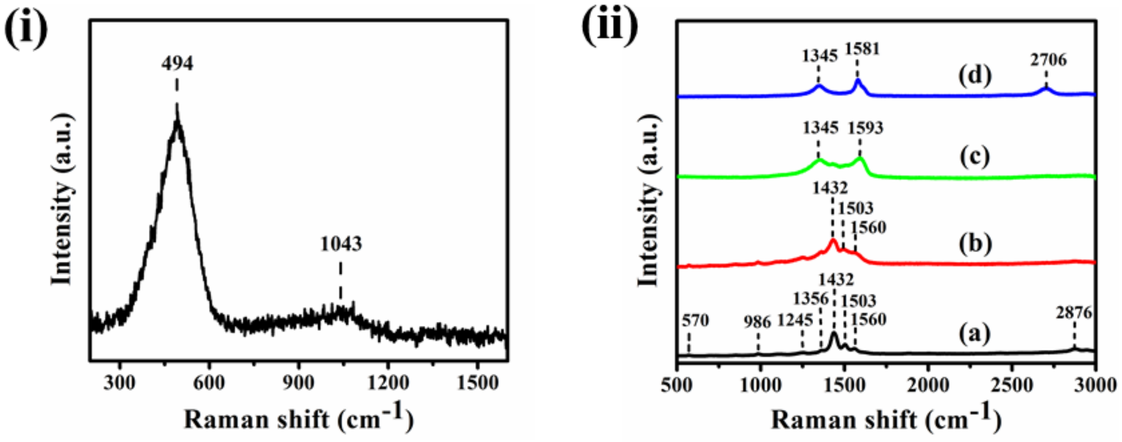

Figure 5.4: *(i) Raman spectrum of NiO and (ii) Raman spectra of (a) PEDOT:PSS, (b) PEDOT:PSS/NiO nanocomposite, (c) rGO/PEDOT:PSS/NiO nanocomposite and (d) rGO.*

5.3.3 X-ray photoelectron spectroscopy

The chemical state and bonding details of as synthesized materials have been analysed by XPS technique and the corresponding spectra are depicted in Figure 5.5. The survey spectrum (Figure 5.5 (i)) shows that nickel (Ni 2p), oxygen (O 1s), carbon (C 1s) and sulphur (S 2p) species are present in rGO/PEDOT:PSS/NiO nanocomposite.

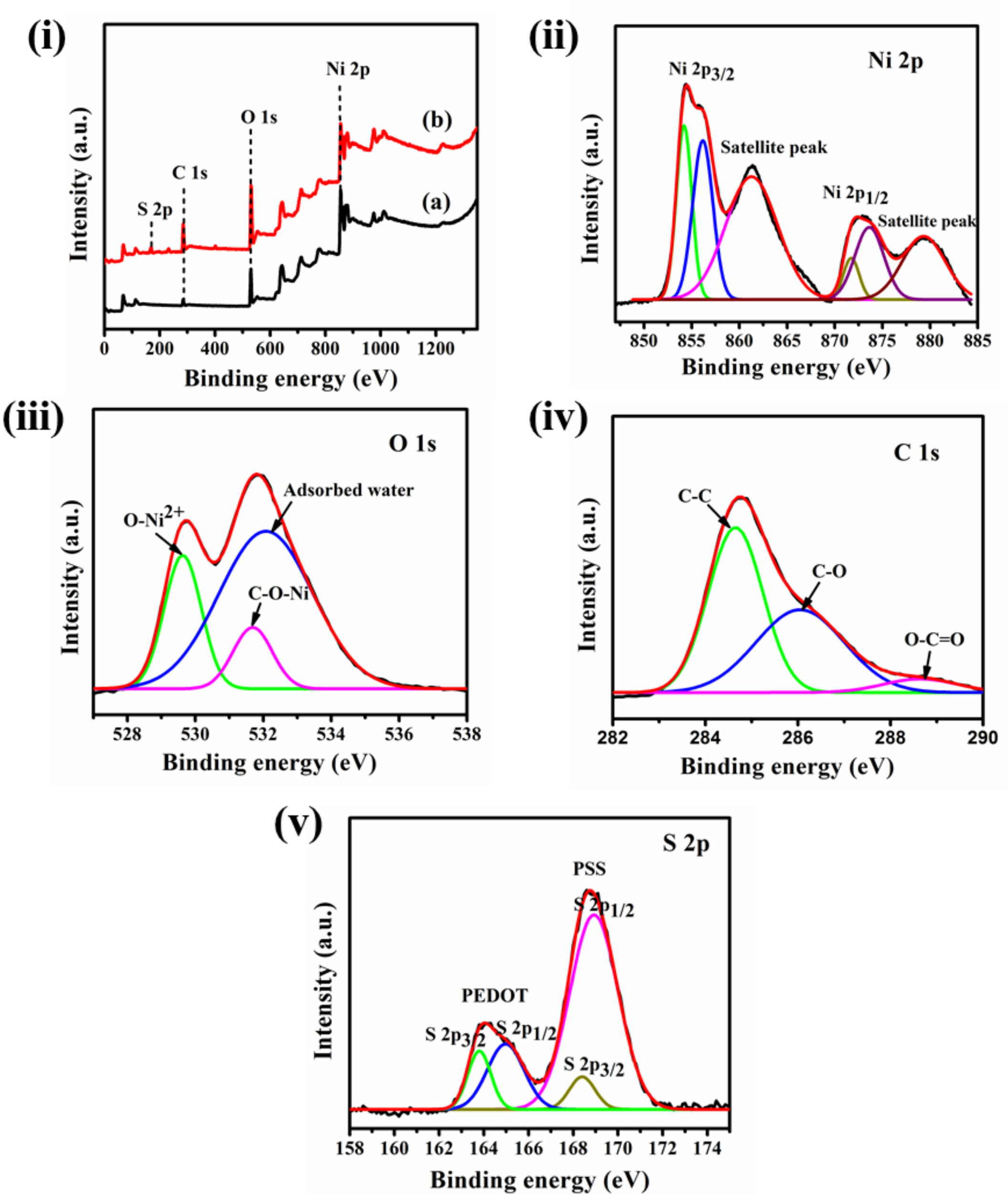

Figure 5.5: *(i) Survey XPS spectra of (a) NiO and (b) rGO/PEDOT:PSS/NiO nanocomposite. Core-level XPS spectra of (ii) Ni 2p, (iii) O 1s, (iv) C 1s and (v) S 2p regions in rGO/PEDOT:PSS/NiO nanocomposite.*

The small intense C 1s peak in survey spectrum of NiO appears due to contamination. The XPS spectra are fitted using Gaussian fitting method. In Ni 2p spectra (Figure 5.5 (ii)), the fitted peaks at binding energies of 854.1 and 871.6 eV correspond to Ni^{2+} and 856.2 and 873.6 eV correspond to Ni^{3+} [35]. On the other hand, shake up peaks of Ni 2p spectra are seen at 879.3 and 861.3 eV of Ni 2p$_{1/2}$ and Ni 2p$_{3/2}$ edge, respectively. In O 1s spectra (Figure 5.5 (iii)), three Gaussian fitted peaks are observed. The sharp peak at

529.6 eV corresponding to O-Ni^{2+} bonds indicate the presence of Ni^{2+} species in the nanocomposite. Moreover, the peaks at 531.6 and 532 eV are assigned to C-O-Ni bond and adsorbed water, respectively. In the Figure 5.5 (iv), deconvoluted C 1s spectrum of rGO/PEDOT:PSS/NiO nanocomposite shows that three different peaks centred at 284.63, 286.04 and 288.67 eV appeared, corresponding to C-C/C=C (sp^2), C-O-C (C-O and C epoxy), O-C=O (C-O) groups, respectively [36]. The strong intense peak of C-C/C=C (sp^2) among all the peaks of C 1s spectrum, indicates the reduction of GO. Furthermore, the existence of sulfur atoms from PEDOT and PSS is confirmed in S 2p spectrum (Figure 5.5 (v)). The deconvoluted peak at 163.8 corresponds to S $2p_{3/2}$ state, while the peak at 165 eV is assigned to S $2p_{1/2}$ state of thiophene ring in PEDOT [31]. The peak at 168.3 eV is related to S $2p_{3/2}$ electronic configuration of sulfonate (SO^{3-}) and peak at 168.9 eV is attributed to S $2p_{1/2}$ state of sulfonic acid groups (SO_3H) in PSS, respectively [31].

5.3.4 Nitrogen (N_2) adsorption-desorption analysis

Figure 5.6 represents the N_2 adsorption-desorption isotherm and corresponding pore size distribution curve has been calculated by BJH method from desorption branch for NiO, PEDOT:PSS/NiO and rGO/PEDOT:PSS/NiO nanocomposites. All the as prepared samples exhibit type IV isotherm according to International Union of Pure and Applied Chemistry (IUPAC) classification with a well-defined H3 hysteresis loop suggesting the mesoporous nature. In Figure 5.6 (i), the loop of NiO appears within the relative pressure range of 0.6-1.0 P/P_0; while the loops of PEDOT:PSS/NiO and rGO/PEDOT:PSS/NiO nanocomposites have been observed within the region of 0.55-1.0 P/P_0 (Figure 5.6 (ii)) and 0.4-1.0 P/P_0 (Figure 5.6 (iii)), respectively indicating the slit-shaped pore structure. Moreover, NiO and PEDOT:PSS/NiO nanocomposite have a large amount of mesopores with a narrow pore size distribution with single peaks at 2.5 nm and 4.2 nm as shown in inset of Figures 5.6 (i) and (ii), respectively and rGO/PEDOT:PSS/NiO nanocomposite possess wider pore size distribution with its peak at 7.4 nm as shown in inset of Figure 5.6 (iii). rGO/PEDOT:PSS/NiO nanocomposite reveals comparatively larger specific surface area (270 $m^2\ g^{-1}$) and higher pore volume (0.79 $cm^3\ g^{-1}$) than that of NiO (87 $m^2\ g^{-1}$ and 0.21 $cm^3\ g^{-1}$) and PEDOT:PSS/NiO nanocomposite (115 $m^2\ g^{-1}$ and 0.44 $cm^3\ g^{-1}$). The large specific surface area and presence of connected pores in rGO/PEDOT:PSS/NiO nanocomposite favour the enhanced methanol oxidation reaction rate due to availability of abundant electroactive sites.

(i)

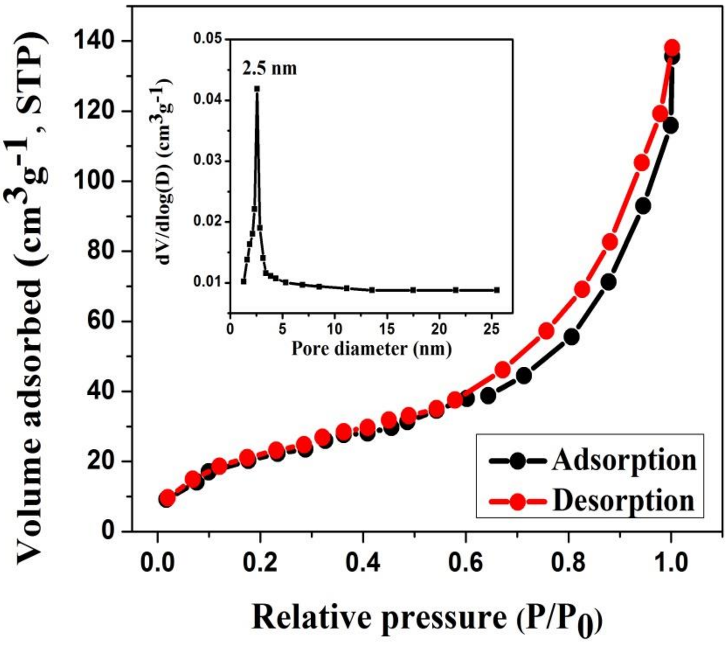

(ii)

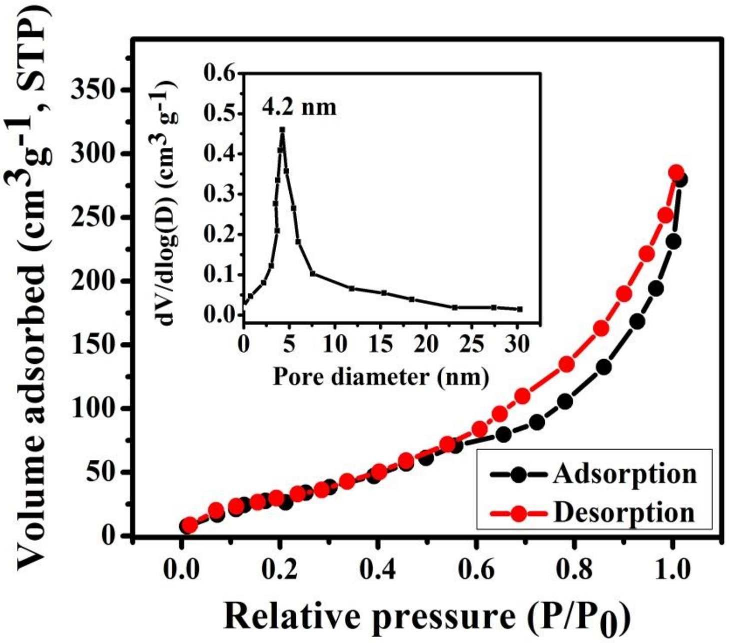

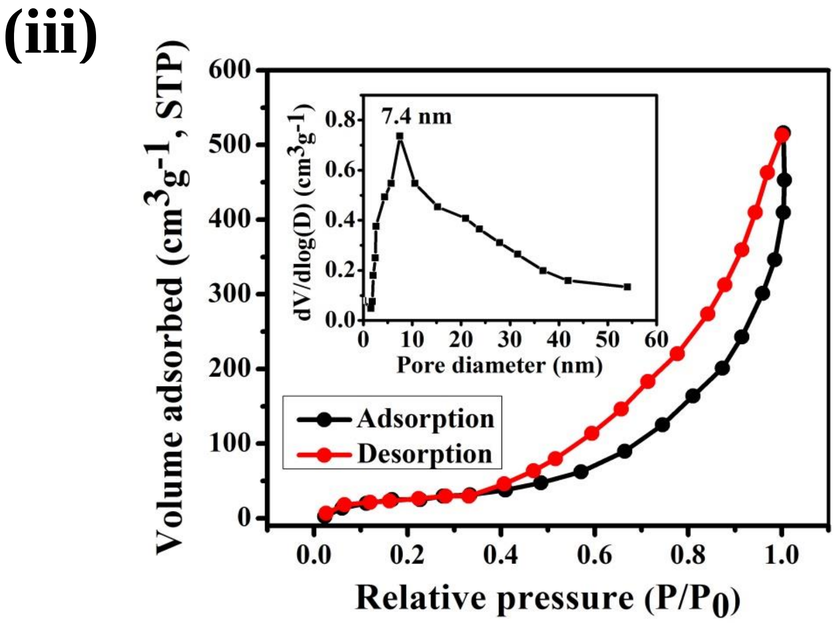

Figure 5.6: *Nitrogen adsorption-desorption isotherms of (i) NiO, (ii) PEDOT:PSS/NiO nanocomposite and (iii) rGO/PEDOT:PSS/NiO nanocomposite. Inset figures show pore size distribution curve.*

5.4 Electrochemical characterizations

5.4.1 Electrochemical activity of the modified electrodes

To investigate the electrochemical behaviours, NiO/ITO, PEDOT:PSS/NiO/ITO and rGO/PEDOT:PSS/NiO/ITO electrodes have been initially tested in bare 0.5 M NaOH electrolyte at a scan rate of 50 mV s^{-1} from -0.08 to +0.5 V (Figure 5.7 (i)). Prior to electrocatalytic investigations, the electrodes have been cycled through 30 potential CV cycles at a sweep rate of 50 mV s^{-1} in 0.5 M NaOH. This has been done to boost the number of hydroxides and oxyhydroxides on catalyst surface, resulting in thickening of the electrocatalytic layers [37]. The current has been normalized to the geometric surface area of ITO electrode. This reveals the appearance of oxidation and reduction peaks around 0.45 and 0.3 V, respectively, attributing to the conversion between Ni^{+2}/ Ni^{+3} binary redox states. At all the modified ITO electrodes, the sharp redox peaks of the surface confined Ni^{2+}/Ni^{3+} have been observed [38].

$$\mathrm{NiO + OH^- \rightarrow NiOOH + e^-} \qquad [5.1]$$

$$\mathrm{Ni(OH)_2 + OH^- \rightarrow NiOOH + H_2O + e^-} \qquad [5.2]$$

It has been observed that the current of rGO/PEDOT:PSS/NiO/ITO electrode at redox peaks are much higher than that of NiO/ITO and PEDOT:PSS/NiO/ITO electrodes, suggesting that rGO/PEDOT:PSS/NiO/ITO electrode possesses higher electrochemical activity than that of pure NiO and PEDOT:PSS/NiO nanocomposite modified ITO electrodes. The potential difference between redox peaks (ΔE_p) reveals electron transfer rate between the surface of electrode and the redox centres [38]. The ΔE_p values of NiO/ITO and PEDOT:PSS/NiO/ITO electrodes are 0.180 V and 0.153 V, respectively that are larger than that of rGO/PEDOT:PSS/NiO/ITO electrode (0.136 V), suggesting that the electron transfer kinetics at rGO/PEDOT:PSS/NiO/ITO electrode is much faster than that of NiO/ITO and PEDOT:PSS/NiO/ITO electrodes.

5.4.1.1 Variation of anodic peak current (I_{pa}) and cathodic peak current (I_{pc}) vs. scan rate (v)

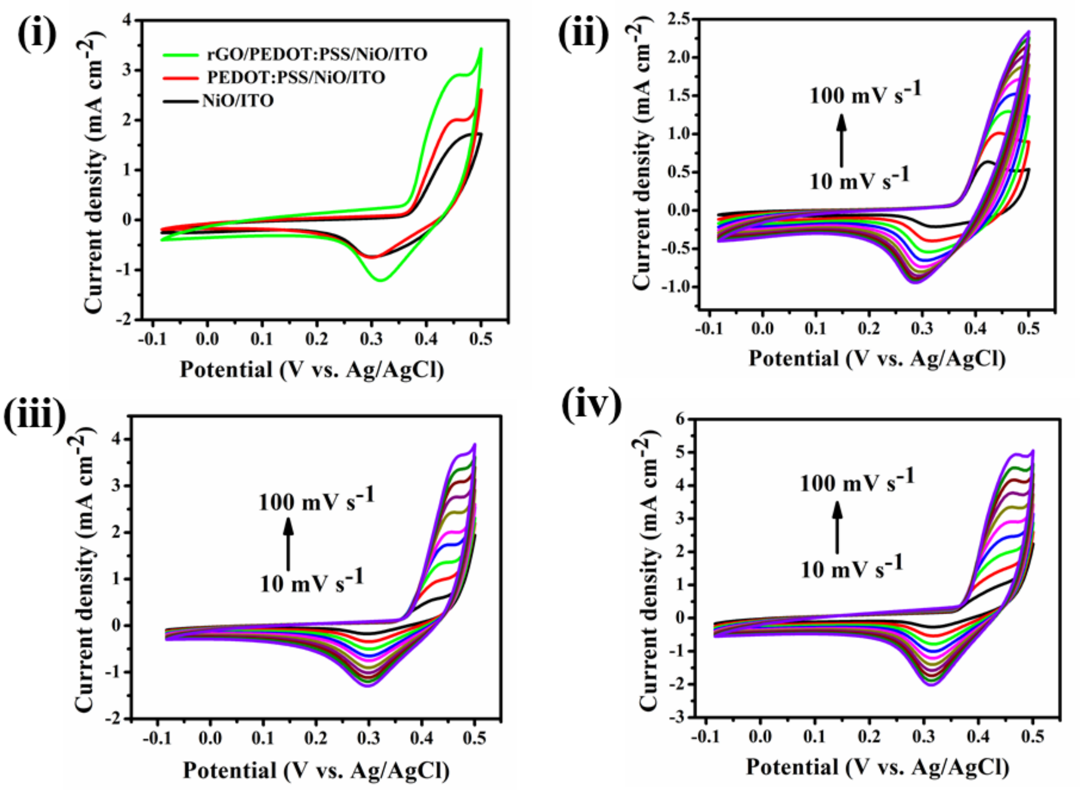

Figure 5.7: *(i) Cyclic voltammograms of NiO/ITO, PEDOT:PSS/NiO/ITO and rGO/PEDOT:PSS/NiO/ITO electrodes in 0.5 M NaOH electrolyte solution at a scan rate of 50 mV s^{-1}. Cyclic voltammograms of (ii) NiO/ITO, (iii) PEDOT:PSS/NiO/ITO and (iv) rGO/PEDOT:PSS/NiO/ITO electrodes at different scan rates (10-100 mV s^{-1}) in 0.5 M NaOH solution.*

The influence of scanning rates on CV response of modified ITO electrodes has also been assessed (Figures 5.7 (ii), (iii) and (iv)). Increasing the scan rate, the anodic peak shifts positively to higher potential side, whereas the cathodic peak shifts toward lower potential side with rise in both anodic and cathodic peak currents. The shift of these peaks occurs as a result of electrochemical polarization causing an increase in internal diffusion resistance of the electrodes and thereby limiting the reaction kinetics. Therefore, at larger scan rates, generation of NiOOH species would be inadequate. Hence, $Ni(OH)_2$/NiOOH transition on Ni based electrodes can be referred as diffusion-controlled process. Moreover, the electron transfer process in the as prepared electrodes is quasi-reversible process. In case of quasi-reversible process, peak to peak separation increases with increase in scan rates [39].

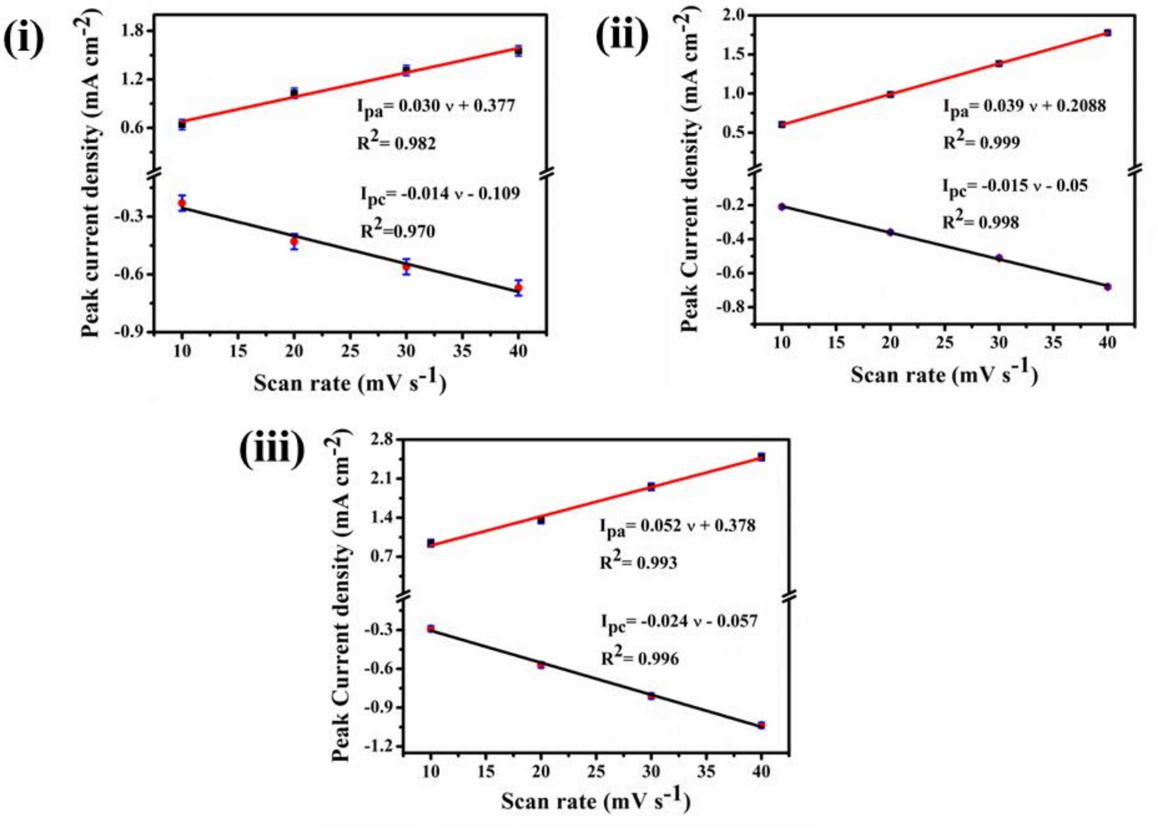

Figure 5.8: *The linear fitted graphs between peak current densities (I_p) and scan rate (ν) (upto 40 mV s^{-1}) for (i) NiO/ITO, (ii) PEDOT:PSS/NiO/ITO and (iii) rGO/PEDOT:PSS/NiO/ITO electrodes.*

The electrochemical activities of redox couples have been investigated from the graph (Figure 5.8) between peak current densities (I_p) and scan rate (ν) (upto 40 mV s^{-1}). Brown-Anson model [40] has been employed to calculate surface coverage (r^*) of the redox couple Ni^{2+}/Ni^{3+} over the surface of electrode as presented below:

$$I_p = \frac{n^2F^2r^*A\nu}{4RT} \qquad [5.3]$$

Where, n is the number of electrons involved in the reaction, A is the area of electrode, and F, R and T have usual meanings. The obtained values of surface coverage of Ni^{2+}/Ni^{3} redox couple over the surface of NiO/ITO, PEDOT:PSS/NiO/ITO and rGO/PEDOT:PSS/NiO/ITO electrodes are 2.35×10^{-8}, 2.89×10^{-8} and 4.07×10^{-8} mol cm^{-2}, respectively. The surface coverage of redox states over rGO/PEDOT:PSS/NiO/ITO electrode is 1.4 folds and 1.7 folds larger than that of PEDOT:PSS/NiO/ITO and NiO/ITO electrodes, respectively. The reason behind the larger surface coverage over rGO/PEDOT:PSS/NiO/ITO electrode is due to the presence of rGO with large numbers of active sites.

The plots of peak current densities vs. square root of scan rate ($\nu^{1/2}$) of NiO/ITO, PEDOT:PSS/NiO/ITO and rGO/PEDOT:PSS/NiO/ITO electrodes in Figure 5.9 show a linear response at larger scan rates (50-100 mV s^{-1}), indicating that the Faradaic reaction follows a diffusion-controlled process. The slope of linear plots of anodic peak currents (I_{pa}) against square roots of scan rate ($\nu^{1/2}$) give diffusion capability of hydroxyl ions. Typically, a higher slope value indicates fast diffusion capability of hydroxyl ions and presence of more electroactive NiOOH species on the electrodes. The anodic slopes of these plots for NiO/ITO, PEDOT:PSS/NiO/ITO and rGO/PEDOT:PSS/NiO/ITO electrodes are calculated to be 0.211, 0.561, and 0.696 respectively. The higher slope value for rGO/PEDOT:PSS/NiO/ITO electrode implies better diffusion capability of hydroxyl ions on the electrode than that of the others, benefiting that large number of NiOOH species formed on the rGO/PEDOT:PSS/NiO/ITO electrode and Ni sites are easily accessible to OH^- as compared to NiO/ITO and PEDOT:PSS/NiO/ITO electrodes [41].

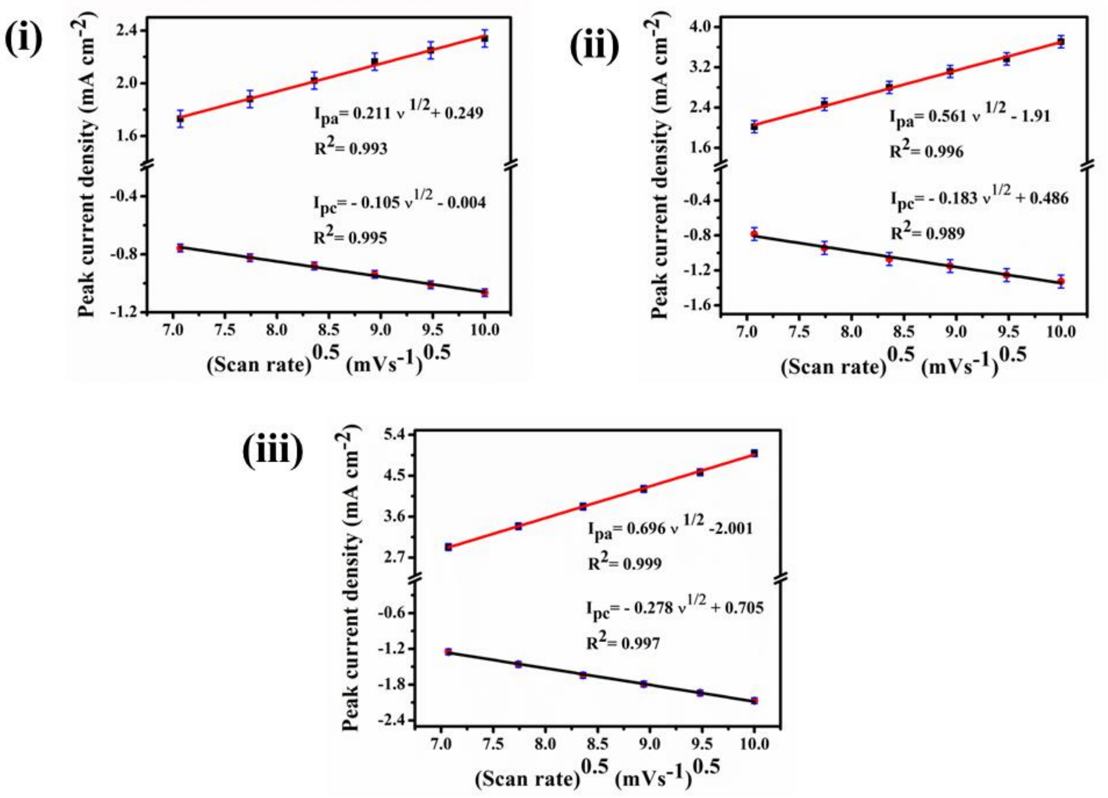

***Figure 5.9:** The linear fitted plots of peak current densities against the square root of scan rate ($v^{1/2}$) of (i) NiO/ITO, (ii) PEDOT:PSS/NiO/ITO and (iii) rGO/PEDOT:PSS/NiO/ITO electrodes.*

5.4.1.2 Variation of anodic peak potential (E_{pa}) and cathodic peak potential (E_{pc}) vs. scan rate (ν)

The graphs for anodic peak voltage (E_{pa}) and cathodic peak voltage (E_{pc}) for the modified electrodes with logarithm of different scan rate (log ν) have been plotted in Figure 5.10. Laviron expression has been employed to find the values of charge transfer coefficient (α) and heterogeneous rate constant (k_s) as shown [42]:

$$E_{pc} = E_0 - 2.3RT\frac{\log\nu}{\alpha nF} \qquad [5.4]$$

$$E_{pa} = E_0 + 2.3RT\frac{\log\nu}{(1-\alpha)nF} \qquad [5.5]$$

$$\log k_s = \alpha\log(1-\alpha) + (1-\alpha)\log\alpha - \log\left(\frac{RT}{nF\nu}\right) - \frac{\alpha(1-\alpha)nF\Delta E_p}{2.3RT} \qquad [5.6]$$

The constants R, T and F in the above equations express their usual meanings, no of electron transfer n =1, ν = scan rate, $\Delta E_p = E_{pa} - E_{pc}$. The values of α_a, α_c and k_s have been tabulated in Table 5.1.

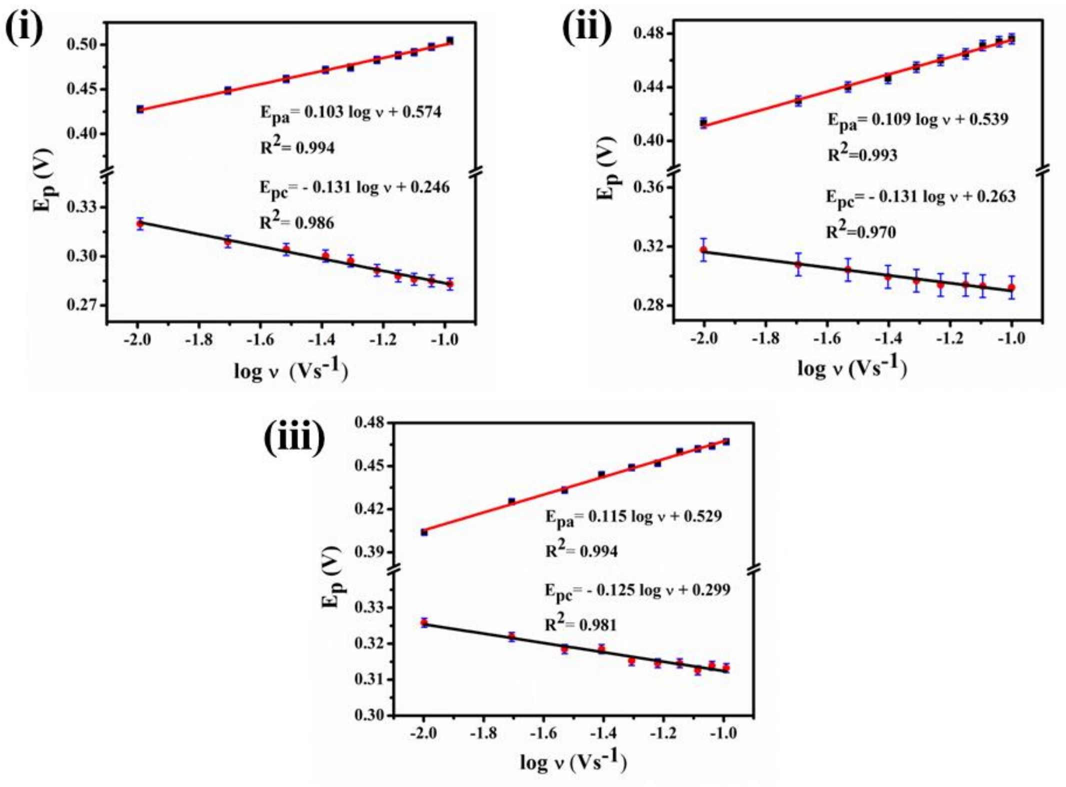

Figure 5.10: *The linear fitted graphs for anodic peak voltage (E_{pa}) and cathodic peak voltage (E_{pc}) with logarithm of different scan rates (log v) for (i) NiO/ITO, (ii) PEDOT:PSS/NiO/ITO and (iii) rGO/PEDOT:PSS/NiO/ITO electrodes.*

Table 5.1: *Calculated values of electron transfer coefficients (both anodic and cathodic) and heterogeneous rate constant of the electrodes.*

Electrodes	Anodic electron transfer coefficient (α_a)	Cathodic electron transfer coefficient (α_c)	Heterogeneous rate constant (k_s) (cm s^{-1})
NiO/ITO	0.43	0.45	0.067
PEDOT:PSS/NiO/ITO	0.46	0.45	0.076
rGO/PEDOT:PSS/NiO/ITO	0.49	0.47	0.089

5.4.2 Electrochemical activity of the electrodes toward methanol oxidation

The CVs of methanol oxidation of the as-prepared electrodes are presented in Figure 5.11 (i). These CV responses show a sharp peak on addition of 0.5 M methanol to the solution, due to oxidation of methanol at the modified electrodes. The availability of unpaired d-electrons or empty d orbitals in NiOOH for formation of bond with absorbed species, contributes to the electrocatalytic activity of NiOOH toward methanol [37]. The Electrooxidation of methanol over the as-synthesized electrodes is shown below:

$$(\mathrm{CH_3OH})_{\mathrm{sol.}} \leftrightarrow (\mathrm{CH_3OH})_{\mathrm{ads}} \tag{5.7}$$

$$(\mathrm{CH_3OH})_{\mathrm{ads}} + \mathrm{NiOOH} \rightarrow (\mathrm{CH_2OH})_{\mathrm{ads}} + \mathrm{Ni(OH)_2} \tag{5.8}$$

$$(\mathrm{CH_2OH})_{\mathrm{ads}} + \mathrm{NiOOH} \rightarrow (\mathrm{CH_2O})_{\mathrm{ads}} + \mathrm{Ni(OH)_2} \tag{5.9}$$

$$(\mathrm{CH_2O})_{\mathrm{ads}} + 2\mathrm{NiOOH} + \mathrm{H_2O} \rightarrow \mathrm{HCOOH} + 2\mathrm{Ni(OH)_2} \tag{5.10}$$

The net reaction can be expressed as [43]:

$$\mathrm{NiOOH} + \mathrm{CH_3OH} + 1.25\ \mathrm{O_2} \rightarrow \mathrm{Ni(OH)_2} + \mathrm{CO_2} + 1.5\ \mathrm{H_2O} \tag{5.11}$$

Fleischmann et al. [44, 45] proposed a mechanism of alcohol oxidation based on the experimental observation and suggested that oxidation of alcohols occurs at that potential in which NiOOH are produced. This mechanism also explains that the amount of $Ni(OH)_2$ increases at the electrode surface during methanol oxidation causing disappearance or decrease in cathodic peak current density in the backward scan at around 300 mV associated with NiOOH/$Ni(OH)_2$ reduction. In backward scan, the amount of regenerated electroactive species NiOOH gradually decreases resulting into decrease in current density due to methanol oxidation [46]. In another work, Taraszewska and Roslonek [47] proposed that penetration of methanol molecules occur through the nickel hydroxide film and then these are oxidized by the hydroxyl ions trapped in the film. When, the as prepared rGO/PEDOT:PSS/NiO/ITO electrode has been dipped into 0.5 M NaOH Solution, the OH^- ions present in the solution react with Ni^{2+} ions to form $Ni(OH)_2$. After that $Ni(OH)_2$ oxidizes to form strong oxidant NiOOH in the forward scan [48, 49]. NiOOH being the electroactive species, oxidizes adsorbed methanol molecules and also it reduces to $Ni(OH)_2$. As shown in above equations [5.9] and [5.10], formaldehyde and formic acid are the intermediates of methanol electrooxidation at Ni-based catalysts. As shown in Figure 5.11 (i), the oxidation peak appears in forward scan due to oxidation of freshly chemisorbed species over the catalyst surface; while the peak during reverse scan arises because of removal of partially carbonaceous intermediates formed during the forward scan [50]. The value of oxidation peak current during forward scan implies the electrocatalytic activity of the electrocatalysts. The current density at rGO/PEDOT:PSS/NiO/ITO electrode (62.6 mA cm^{-2}) is about 5.7 folds and 2 folds larger in comparison to NiO/ITO (10.8 mA cm^{-2}) and PEDOT:PSS/NiO/ITO (30.4 mA cm^{-2}) electrodes, respectively. These results reveal that rGO/PEDOT:PSS/NiO/ITO electrode displays a remarkably higher electrocatalytic activity in comparison to NiO/ITO and

PEDOT:PSS/NiO/ITO electrodes for methanol oxidation reaction in alkaline media. The enhanced electrocatalytic activity can be explained using the following facts: (i) the high electrocatalytic activity of NiO and its conversion to NiOOH that acts as the active sites for combination of methanol; (ii) presence of numerous pores in the nanocomposite enhances the surface area of the electrode material. This is advantageous for contact between the electrode and electrolyte, and also decreases in length of diffusion for the movement of ions and the electrons; (iii) rGO/PEDOT:PSS/NiO nanocomposite has high specific surface area owing to the both nanoplate and nanorod-like structures of NiO, which enables it to act as an excellent methanol oxidation catalyst in the alkaline solution; (iv) in one-dimensional nanorod structure, the transfer of charge between electrode and active sites is enhanced; (v) the large surface area of rGO present in rGO/PEDOT:PSS/NiO nanocomposite enhances the adsorption of methanol molecules while the excellent electrical conductivity of rGO favours the good electrocatalytic activity of the electrode.

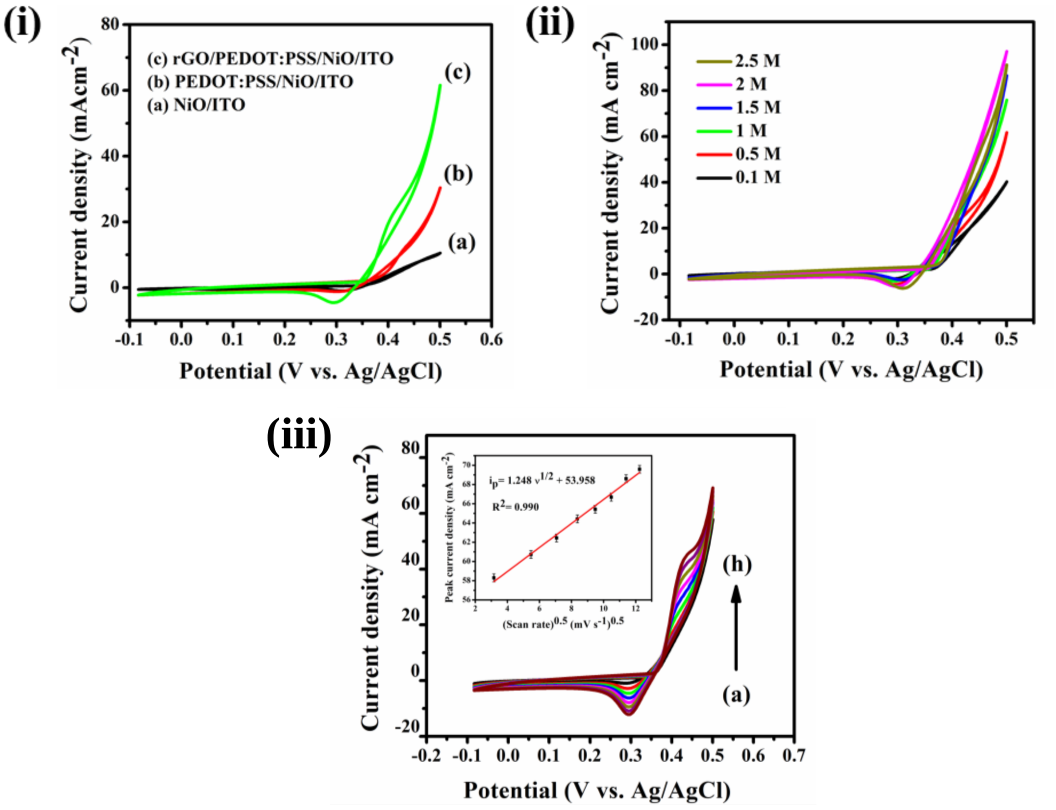

Figure 5.11: *(i) Cyclic voltammograms of (a) NiO/ITO, (b) PEDOT:PSS/NiO/ITO and (c) rGO/PEDOT:PSS/NiO/ITO electrodes in presence of 0.5 M methanol containing in 0.5 M NaOH electrolyte solution at a scan rate 50 mV s^{-1}; (ii) Cyclic voltammograms of rGO/PEDOT:PSS/NiO/ITO electrode in 0.5 M NaOH electrolyte solution containing 0.1*

M, 0.5 M, 1 M, 1.5 M, 2 M and 2.5 M of methanol at a scan rate of 50 mV s^{-1}*; (iii) Cyclic voltammograms of rGO/PEDOT:PSS/NiO/ITO electrode in presence of 0.5 M methanol containing in 0.5 M NaOH electrolyte solution at various scan rates (a) 10 mV* s^{-1}*, (b) 30 mV* s^{-1}*, (c) 50 mV* s^{-1}*,(d) 70 mV* s^{-1}*, (e) 90 mV* s^{-1}*, (f) 110 mV* s^{-1}*, (g) 130 mV* s^{-1} *and (h) 150 mV* s^{-1} *and inset figure shows corresponding plot between anodic peak current density and square root of scan rate.*

As presented in Figure 5.11 (ii), the effect of methanol concentration has been studied on oxidation current within the concentration range from 0.1 M to 2.5 M methanol taking 0.5 M NaOH as supporting electrolyte. Initially, oxidation of NiO on the electrode surface forms NiOOH, which acts as the redox active sites during methanol oxidation. Further, NiOOH combines with methanol molecules for oxidation reaction. Moreover, there is linear increase in oxidation peak current density from 40 to 97 mA cm^{-2} (Figure 5.11 (ii)) on increase in methanol concentration from 0.1 to 2 M due to diffusion controlled process. More methanol molecules come in contact with the active sites (NiOOH) and release more numbers of electrons, and thereby increasing the electrocatalytic activity. Although, oxidation current decreases as the methanol concentration reaches 2.5 M. At a very high methanol concentration, there are no more available active sites on the catalyst surface. Therefore, the optimum methanol concentration is 2 M at rGO/PEDOT:PSS/NiO/ITO electrode i.e. upto this much concentration enough active sites are available for electrochemical reaction. The onset voltage slightly shifts to positive direction beyond 2M concentration of methanol. When the concentration of methanol is as high as 2.5 M, all the active sites are occupied causing decrease in current density.

To reveal information about the kinetics of methanol oxidation at rGO/PEDOT:PSS/NiO/ITO electrode, CV has been performed at various scan rates (Figure 5.11 (iii)). With increase in scan rate, the oxidation peak current density grows accordingly and plot between the oxidation peak current density and the square root of scan rate yields a straight line (inset of Figure 5.11 (iii)), suggesting that methanol oxidation process is diffusion controlled at rGO/PEDOT:PSS/NiO/ITO electrode.

5.4.3 Linear sweep voltammetry and Tafel analysis

Linear sweep voltammograms (LSVs) (Figure 5.12(i)) have been analysed to understand the methanol oxidation activities at NiO/ITO, PEDOT:PSS/NiO/ITO and rGO/PEDOT:PSS/NiO/ITO electrodes measured at a scan rate of 1 mV s^{-1} in a solution of 0.5 M methanol containing in 0.5 M NaOH. The Tafel slope (β), electron transfer coefficient (α) and exchange current density (i_0) have been obtained from Tafel plots (Figure 5.12 (ii)), and listed in Table 5.2. Generally, a smaller Tafel slope indicates that the electrocatalytic oxidation reaction can occur more easily. The Tafel slope (73 mV dec^{-1}) for rGO/PEDOT:PSS/NiO/ITO electrode is smaller than that of NiO/ITO, PEDOT:PSS/NiO/ITO electrodes, suggesting that rGO/PEDOT:PSS/NiO/ITO electrode can facilitate methanol oxidation reaction more easily as compared to PEDOT:PSS/NiO/ITO and NiO/ITO electrodes. The above results confirm faster kinetics of rGO/PEDOT:PSS/NiO/ITO electrode towards methanol oxidation in comparison to PEDOT:PSS/NiO/ITO and NiO/ITO electrodes.

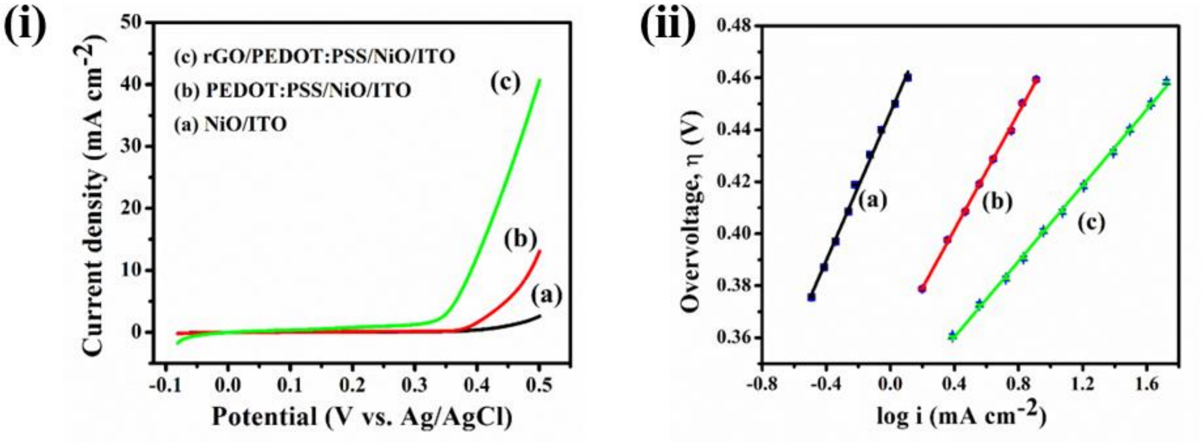

Figure 5.12: *(i) Linear sweep voltammetry curves of (a) NiO/ITO, (b) PEDOT:PSS/NiO/ITO and (c) rGO/PEDOT:PSS/NiO/ITO electrodes recorded at a scan rate of 1 mV s^{-1} in mixed electrolyte solution of 0.5 M NaOH and 0.5 M methanol. (ii) Tafel plots of (a) NiO/ITO, (b) PEDOT:PSS/NiO/ITO and (c) rGO/PEDOT:PSS/NiO/ITO electrodes.*

Table 5.2: *Values of Tafel slope, electron transfer coefficient and exchange current density from Tafel plot of the modified electrodes.*

Electrodes	Tafel slope (β) (mV dec^{-1})	Electron transfer coefficient (α)	Exchange current density (i_o) (mA cm^{-2})
NiO/ITO	142	0.42	7.15×10^{-4}
PEDOT:PSS/NiO/ITO	112	0.53	3.02×10^{-3}
rGO/PEDOT:PSS/NiO/ITO	73	0.81	2.86×10^{-2}

5.4.4 Chronoamperometry and Cyclic stability test

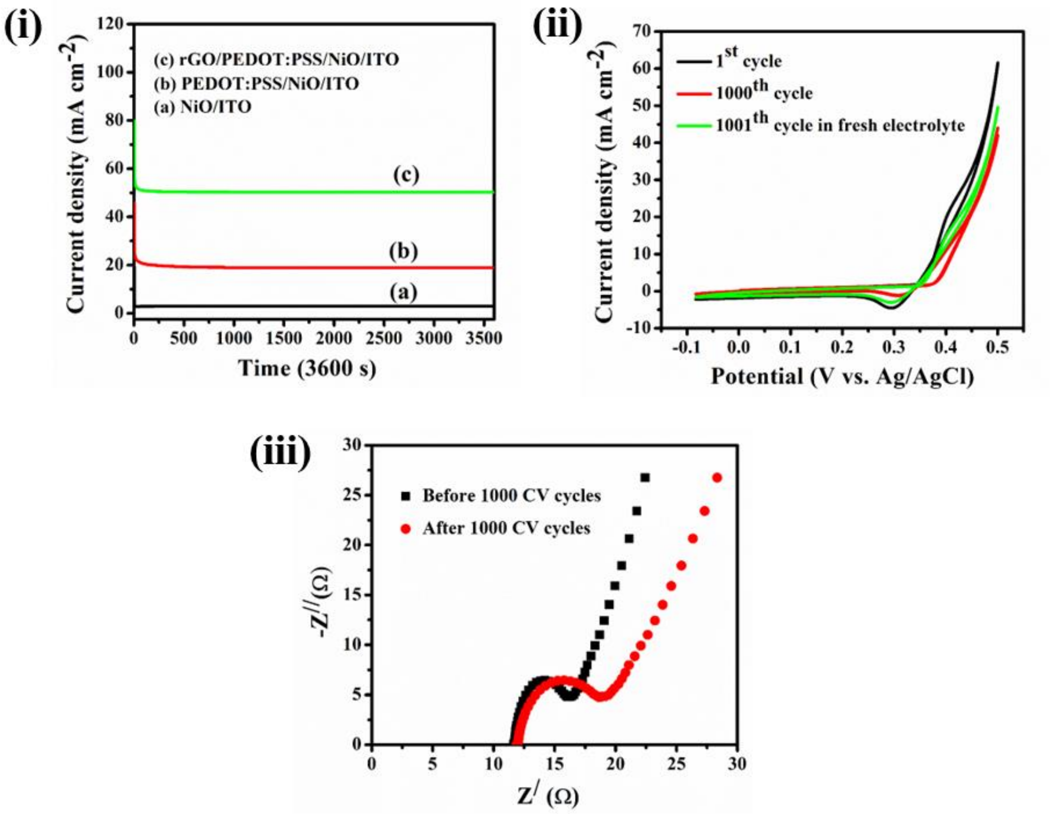

Figure 5.13: *(i) Chronoamperometric curves of (a) NiO/ITO, (b) PEDOT:PSS/NiO/ITO and (c) rGO/PEDOT:PSS/NiO/ITO electrodes in 0.5 M methanol containing in 0.5 M NaOH at an applied potential 0.34 V; (ii) Cyclic stability of rGO/PEDOT:PSS/NiO/ITO electrode for 1000 CV cycles in 0.5 M methanol containing in 0.5 M NaOH at a scan rate 50 mV* s^{-1}*. (iii) EIS curves of rGO/PEDOT:PSS/NiO/ITO electrode in 0.5 M methanol containing in 0.5 M NaOH before and after 1000 CV cycles.*

The chronoamperometric tests have been carried out in 0.5 M methanol containing in 0.5 M NaOH electrolyte at a potential of 0.34 V (vs. Ag/AgCl) for 1 h and the curves have been presented in Figure 5.13 (i). A distinct decrease in current is observed for NiO/ITO, PEDOT:PSS/NiO/ITO and rGO/PEDOT:PSS/NiO/ITO electrodes with 16.6%, 43.4% and 62% retention of initial current. During methanol oxidation, some poisonous intermediates are formed that block the electrode surface causing fast decrease in current. The current at rGO/PEDOT:PSS/NiO/ITO electrode during methanol oxidation is maintained the highest even after long time operation, which is 50.7 mA cm^{-2} in comparison to 19.5 and 3.2 mA cm^{-2} obtained at PEDOT:PSS/NiO/ITO and NiO/ITO electrodes, respectively. The experimental results indicate that rGO/PEDOT:PSS/NiO electrode is stable and poisoning-tolerant in alkaline medium. The stability of rGO/PEDOT:PSS/NiO/ITO electrode has also been investigated using continuous CV cycles (Figure 5.13 (ii)). rGO/PEDOT:PSS/NiO/ITO exhibits current retention 71% of initial cycle after 1000 CV cycles at 50 mV s^{-1}. On replacing the old electrolyte with fresh one, the current density becomes 80% of initial value. Hence, the decrease in current may be due to methanol consumption at the electrode surface. Moreover, the current decay in CA and CV tests can also be attributed to NiO impurity, mainly, micro cracking and disintegration and related to the generation of NiOOH/Ni(OH)$_2$ redox state.

5.4.5 Electrochemical impedance spectroscopy measurements after cyclic Stability test

The EIS curves of rGO/PEDOT:PSS/NiO/ITO electrode in 0.5 M methanol containing in 0.5 M NaOH before and after stability test between the frequency range of 0.1 Hz to 10 MHz are shown in Figure 5.13 (iii). The diameter of semicircle in EIS curve represents interface ionic charge transfer resistance [51]. The ionic charge transfer resistance at the rGO/PEDOT:PSS/NiO/ITO electrode increases from 4.52 Ω to 6.96 Ω after stability test for 1000 CV cycles due to formation of intermediates over the electrode surface.

5.4.6 Characterizations after cyclic stability test

To investigate morphology, structure and composition of the electrode material after 1000 CV cycles, TEM, XRD, and XPS measurements have been performed of rGO/PEDOT:PSS/NiO/ITO electrode. The morphology of rGO/PEDOT:PSS/NiO nanocomposite after 1000 CV cycles has been examined by TEM (Figures 5.14 (i) and (ii)). The TEM images of rGO/PEDOT:PSS/NiO nanocomposite reveal the coexistence of NiO nanorod and nanoplate structure even after 1000 CV cycles. After continuous CV cycling, the diameter of NiO nanoplate lie within the range from 46 to 53 nm indicating aggregation (shown in red circles in Figure 5.14 (i)) of the nanoplates, while the length of NiO nanorods are shortened and the lengths lie within 30 to 40 nm. The XRD pattern of rGO/PEDOT:PSS/NiO/ITO electrode recorded after 1000 CV cycles in Figure 5.14 (ii) shows that the intensities of characteristic peaks of rGO/PEDOT:PSS/NiO nanocomposite decrease indicating small loss of crystallinity of the nanocomposite, however no new phase is formed after cycling test. Moreover, the ITO peaks appear at 30.4°, 35.6°, 50.7° and 60.4° are associated with (222), (400), (440) and (622) planes respectively.

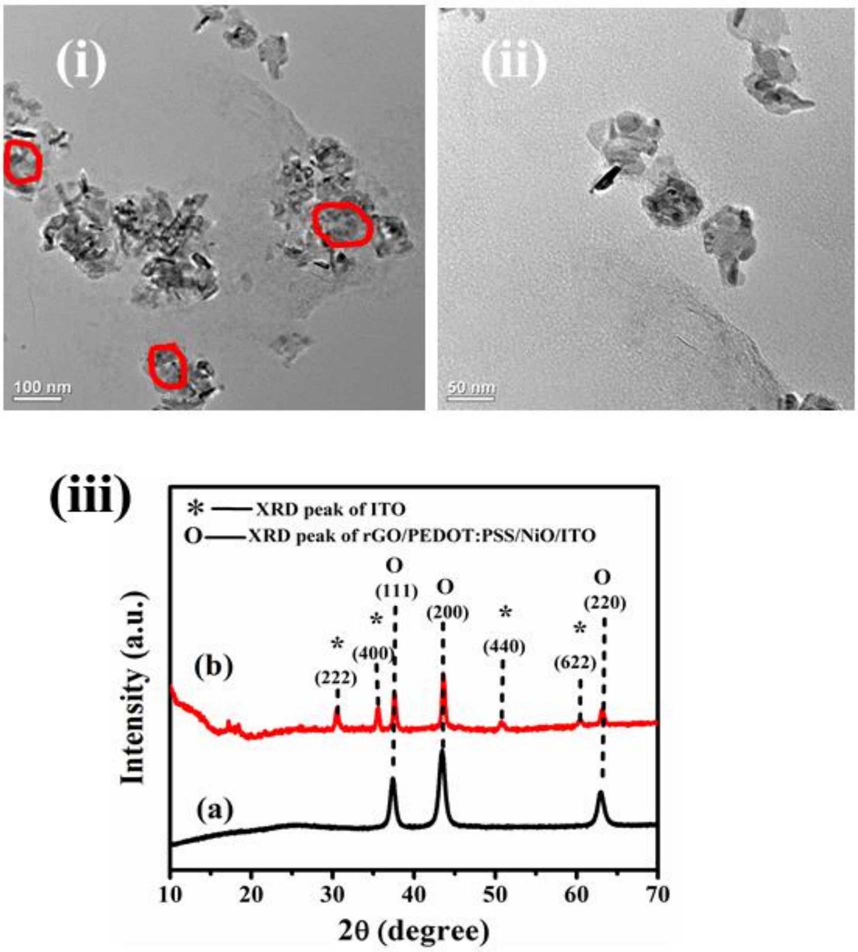

Figure 5.14: *TEM micrographs of rGO/PEDOT:PSS/NiO nanocomposite after 1000 CV cycles in 0.5 M methanol containing in 0.5 M NaOH solution at resolutions of (i) 100 nm and (ii) 50 nm, (iii) XRD patterns of (a) rGO/PEDOT:PSS/NiO nanocomposite and (b) rGO/PEDOT:PSS/NiO/ITO electrode after 1000 CV cycles in 0.5 M methanol containing in 0.5 M NaOH.*

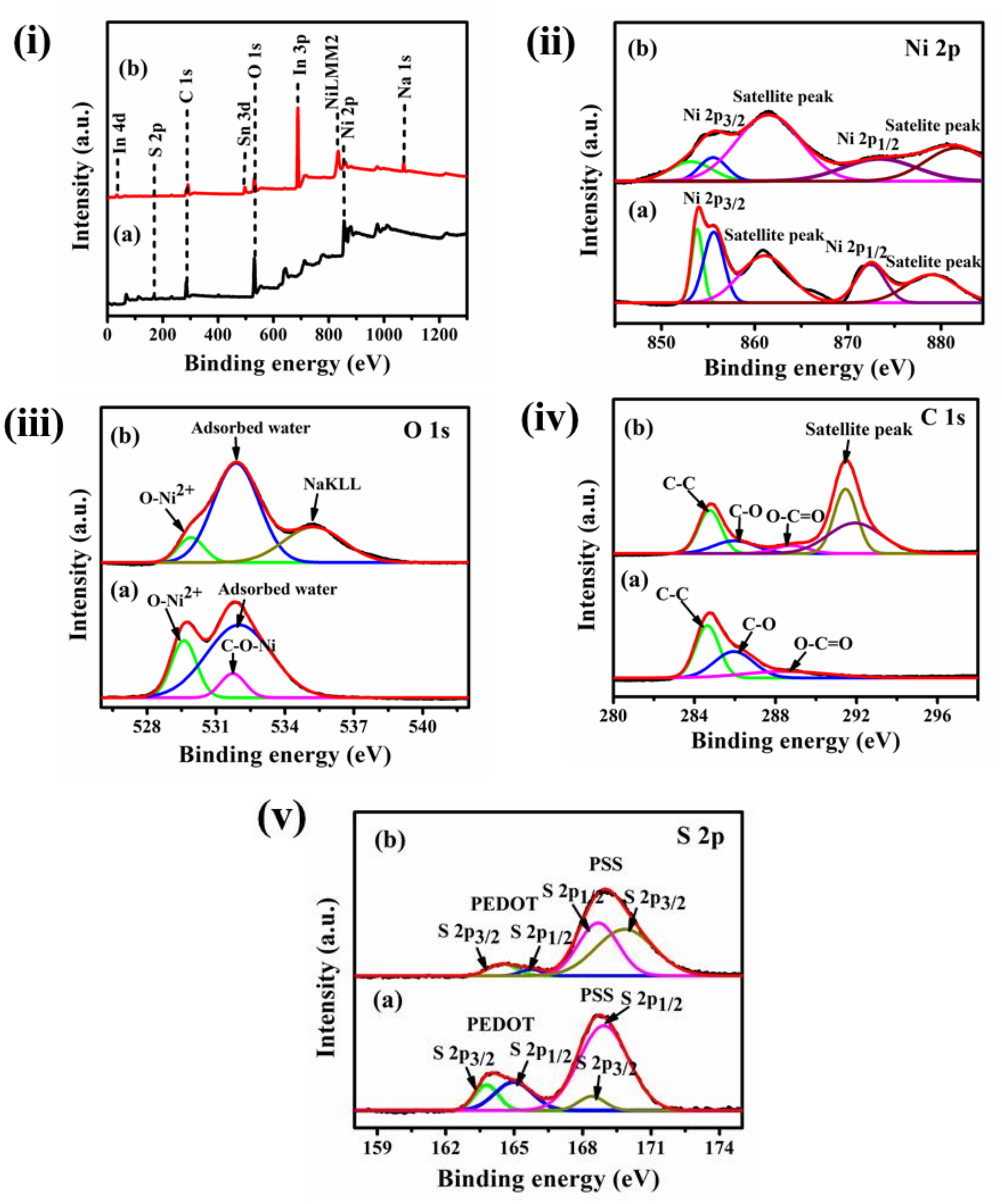

Figure 5.15: *(i) Survey spectra of (a) rGO/PEDOT:PSS/NiO nanocomposite (b) rGO/PEDOT:PSS/NiO/ITO electrode after 1000 CV cycles. Core-level XPS spectra of (ii) Ni 2p, (iii) O 1s, (iv) C 1s (v) S 2p regions of (a) rGO/PEDOT:PSS/NiO nanocomposite (b) rGO/PEDOT:PSS/NiO/ITO electrode after 1000 CV cycles in 0.5 M methanol containing in 0.5 M NaOH solution.*

The XPS measurements of rGO/PEDOT:PSS/NiO nanocomposite before stability test and rGO/PEDOT:PSS/NiO/ITO electrode after stability test for 1000 CV cycles in 0.5M methanol containing in 0.5 M NaOH solution have been plotted in Figure 5.15 (i)-(v).

rGO/PEDOT:PSS/NiO/ITO electrode exhibits several XPS peaks associated with In3p, Sn3d, and In4d bands, attributing to ITO substrate used as shown in survey spectrum (Figure 5.15 (i)) [52]. After stability test, the deconvoluted Ni 2p spectrum (Figure 5.15 (ii)) shows decrease in intensities of peaks at 854.1 eV corresponding to Ni^{2+} oxidation state and at 856.2 eV related to Ni^{3+} state. Moreover, the intensity of peak at 872.6 eV assigning to Ni^{2+} and Ni^{3+} oxidation state is also diminished, however the intensities of satellite peaks are same even after stability test. During electrochemical reaction of rGO/PEDOT:PSS/NiO/ITO electrode, continuous transition between $Ni(OH)_2$/NiOOH occurs and they act as electroactive media during methanol oxidation reaction. Hence, the consumption of these Ni species during continuous CV cycles causes decrease in intensities of characteristic peaks in Ni 2p spectrum. In O 1s spectrum (Figure 5.15 (iii)), the intensity of deconvoluted peak at 529.6 eV corresponding to $O-Ni^{2+}$ bonds decreases due to consumption of Ni^{2+} ions during methanol oxidation and a much broader peak appears at 535.1 eV after stability test, which can be attributed to sodium Auger peak (NaKLL) due to a significant amount of Na^+ on the electrode surface. The intensity of main peak of C 1s spectrum (Figure 5.15 (iv)) decreases indicating depletion of carbon in rGO/PEDOT:PSS/NiO/ITO electrode and also a satellite peak appears at 291.4 eV. In S 2p spectrum (Figure 5.15 (v)), the intensity of peak related to PEDOT slightly decreases due to disintegration of polymer film after continuous CV cycles. A small intense peak at 1071 eV is observed in the survey spectrum (Figure 5.15 (i)) of rGO/PEDOT:PSS/NiO/ITO electrode after stability test suggesting the adsorption of Na^+ ions from the electrolyte onto the surface of electrode.

5.5 Summary

In this work, coexistence of NiO nanoplate and nanorod structures have been observed in TEM micrographs, which have been further coated with PEDOT:PSS and embedded in rGO nanosheets. The large number of electroactive sites existing at the surface of two dimensional NiO nanoplate and additional active sites at the interface with one dimensional NiO nanorod offer optimum electrochemical performances. A larger methanol oxidation current density of 62.6 mA cm^{-2} and lower onset voltage of 0.34 V have been obtained at rGO/PEDOT:PSS/NiO/ITO electrode at a scan rate of 50 mV s^{-1} in presence of 0.5 M methanol containing in 0.5 M NaOH electrolyte. A saturation current density of 97.4 mA cm^{-2} has been obtained for 2 M of methanol at a scan rate of

50 mV s^{-1}. The smaller Tafel slope of 73 mV dec^{-1} and higher exchange current density of 2.86×10^{-2} mA cm^{-2} at rGO/PEDOT:PSS/NiO/ITO electrode indicates faster electrooxidation kinetics of methanol. The chronoamperometry results show a higher current retention of 62% for 1 h and cyclic stability measurements for 1000 CV cycles reveal 71% retention of initial cycle at rGO/PEDOT:PSS/NiO/ITO electrode. The TEM micrographs of rGO/PEDOT:PSS/NiO nanocomposite after cyclic stability test for 1000 CV cycles reveal aggregation of NiO nanoplates and decrease in length of NiO nanorods. The decrease in intensity of characteristic XRD peaks of rGO/PEDOT:PSS/NiO/ITO electrode after continuous CV cycling suggests the loss of crystallinity of the nanocomposite. The appearance of small intense peak at 1071 eV in the survey spectra of rGO/PEDOT:PSS/NiO/ITO electrode indicates the adsorption of Na^+ ions from the electrolyte onto the surface of electrode. The decrease in intensities of core level spectra of Ni 2p, C 1s, O 1s and S 2p peak after continuous 1000 CV cycles implies consumption of nickel species, depletion of carbon and disintegration of PEDOT:PSS film, respectively.

The superior methanol oxidation activity of rGO/PEDOT:PSS/NiO/ITO electrode can be ascribed to the following facts: (i) the NiO nanorod-nanoplate hybrid structure with high electrical conductivity increases the electron transfer rate; (ii) hydrophilic property of hydroxylated surface facilitates methanol oxidation reaction and (iii) the rGO nanosheets with large surface area, good electrical conductivity and chemical stability, provides a good support for methanol oxidation reactions. The present work not only establishes a non-precious electrocatalyst but also reports a facile and affordable synthesis strategy of ternary nanocomposite of NiO, PEDOT:PSS and rGO nanosheets.

5.6 References

[1] Jana, J., Bhamu, K.C., Ngo, Y.L.T., Kang, S.G., Chung, J.S. and Hur, S.H. Designing a bimetallic transition metal oxide/hydroxide composite for effective electrocatalytic oxygen evolution reaction. *Applied Surface Science*, 562:150253, 2021.

[2] Alvarenga, G.M. and Villullas, H.M. Transition metal oxides in the electrocatalytic oxidation of methanol and ethanol on noble metal nanoparticles. *Current Opinion in Electrochemistry*, 4(1):39-44, 2017.

[3] Elakkiya, R., Mathankumar, S. and Maduraiveeran, G. Design of transition metal oxides nanosheets for the direct electrocatalytic oxidation of glucose. *Materials Chemistry and Physics*, 269:124770, 2021.

[4] Lei, Z., Lee, J.M., Singh, G., Sathish, C.I., Chu, X., Ala'a, H., Vinu, A. and Yi, J. Recent advances of layered-transition metal oxides for energy-related applications. *Energy Storage Materials*, 36:514-550, 2021.

[5] Yao, M., Hu, Z., Xu, Z., Liu, Y., Liu, P. and Zhang, Q. Template synthesis and characterization of nanostructured hierarchical mesoporous ribbon-like NiO as high performance electrode material for supercapacitor. *Electrochimica Acta*, 158:96-104, 2015.

[6] Qu, H.Y., Primetzhofer, D., Arvizu, M.A., Qiu, Z., Cindemir, U., Granqvist, C.G. and Niklasson, G.A. Electrochemical rejuvenation of anodically coloring electrochromic nickel oxide thin films. *ACS applied materials & interfaces*, 9(49):42420-42424, 2017.

[7] Li, Z., Niu, W., Zhou, L. and Yang, Y. Phosphorus and aluminum codoped porous NiO nanosheets as highly efficient electrocatalysts for overall water splitting. *ACS Energy Letters*, 3(4):892-898, 2018.

[8] Annadurai, K., Sudha, V., Murugadoss, G. and Thangamuthu, R. Electrochemical sensor based on hydrothermally prepared nickel oxide for the determination of 4-acetaminophen in paracetamol tablets and human blood serum samples. *Journal of Alloys and Compounds*, 852:156911, 2021.

[9] Ruan, X., Yang, Y., Pu, K., Gao, M., Liu, Y. and Pan, H. Superior long-term cyclability of a nanocrystalline NiO anode enabled by a mechanochemical reaction-induced amorphous protective layer for Li-ion batteries. *Journal of Power Sources*, 397:134-142, 2018.

[10] Yang, W., Yang, X., Jia, J., Hou, C., Gao, H., Mao, Y., Wang, C., Lin, J. and Luo, X. Oxygen vacancies confined in ultrathin nickel oxide nanosheets for enhanced electrocatalytic methanol oxidation. *Applied Catalysis B: Environmental*, 244:1096-1102, 2019.

[11] George, G. and Anandhan, S. Synthesis and characterisation of nickel oxide nanofibre webs with alcohol sensing characteristics. *Rsc Advances*, 4(107):62009-62020, 2014.

[12] Zhang, X., Shi, W., Zhu, J., Zhao, W., Ma, J., Mhaisalkar, S., Maria, T.L., Yang, Y., Zhang, H., Hng, H.H. and Yan, Q. Synthesis of porous NiO nanocrystals with controllable surface area and their application as supercapacitor electrodes. *Nano Research*, 3(9):643-652, 2010.

[13] Chinnappan, A., Dongxiao, J., Jayathilaka, W.A.D.M., Baskar, C., Qin, X. and Ramakrishna, S. Facile synthesis of electrospun C@ NiO/Ni nanofibers as an electrocatalyst for hydrogen evolution reaction. *International Journal of Hydrogen Energy*, 43(32):15217-15224, 2018.

[14] Zhang, T., Wu, M.Y., Yan, D.Y., Mao, J., Liu, H., Hu, W.B., Du, X.W., Ling, T. and Qiao, S.Z. Engineering oxygen vacancy on NiO nanorod arrays for alkaline hydrogen evolution. *Nano Energy*, 43:103-109, 2018.

[15] Ensafi, A.A., Afiuni, S.S. and Rezaei, B. NiO nanoparticles decorated at Nile blue-modified reduced graphene oxide, new powerful electrocatalysts for water splitting. *Journal of Electroanalytical Chemistry*, 816:160-170, 2018.

[16] Wang, P., Zhang, X., Wei, Y. and Yang, P. Ni/NiO nanoparticles embedded inporous graphite nanofibers towards enhanced electrocatalytic performance. *International Journal of Hydrogen Energy*, 44(36):19792-19804, 2019.

[17] Yang, W., Wei, A., Liu, J., Xiao, Z., Zhao, Y. and Zhang, Y. Rational construction of vertical few layer graphene/NiO core-shell nanoflake arrays for efficient oxygen evolution reaction. *Materials Research Bulletin*, 139, 111260, 2021.

[18] Zhao, Y., Zhang, Y., Ding, Y. and Chen, M. Hexagonal nanoplates of NiO/CoO/Fe_2O_3 composite acting as an efficient photocatalytic and electrocatalytic water oxidation catalyst. *Dalton Transactions*, 44(35):15628-15635, 2015.

[19] Li, W., Song, Z., Deng, X., Fu, X.Z. and Luo, J.L. Decoration of NiO hollow spheres composed of stacked nanosheets with CeO_2 nanoparticles: enhancement

effect of CeO_2 for electrocatalytic methanol oxidation. *Electrochimica Acta*, 337:135684, 2020.

[20] Mondal, A., Paul, A., Srivastava, D.N. and Panda, A.B. NiO hollow microspheres as efficient bifunctional electrocatalysts for overall water-splitting. *International Journal of Hydrogen Energy*, 43(47):21665-21674, 2018.

[21] Li, W., Bu, Y., Jin, H., Wang, J., Zhang, W., Wang, S. and Wang, J. The preparation of hierarchical flowerlike NiO/reduced graphene oxide composites for high performance supercapacitor applications. *Energy & fuels*, 27(10):6304-6310, 2013.

[22] Zhou, G., Wang, D.W., Yin, L.C., Li, N., Li, F. and Cheng, H.M. Oxygen bridges between NiO nanosheets and graphene for improvement of lithium storage. *ACS nano*, 6(4):3214-3223, 2012.

[23] Baruah, B. and Deb, P. Performance and application of carbon-based electrocatalysts in direct methanol fuel cell. *Materials Advances*, 2(16):5344-5364, 2021.

[24] Kumar, J.P., Giri, S.D. and Sarkar, A. Mesoporous NiO with different morphology: Synthesis, characterization and their evaluation for oxygen evolution reaction. *International Journal of Hydrogen Energy*, 43(33):15639-15649, 2018.

[25] Behera, S.K., Deb, P. and Ghosh, A. Mechanistic study on electrocatalytic hydrogen evolution by high efficiency graphene/MoS_2 heterostructure. *ChemistrySelect*, 2(13):3657-3667, 2017.

[26] Chemchoub, S., Oularbi, L., El Attar, A., Younssi, S.A., Bentiss, F., Jama, C. and El Rhazi, M. Cost-effective non-noble metal supported on conducting polymer composite such as nickel nanoparticles/polypyrrole as efficient anode electrocatalyst for ethanol oxidation. *Materials Chemistry and Physics*, 250:123009, 2020.

[27] Askari, M.B., Salarizadeh, P., Seifi, M. and Rozati, S.M. Ni/NiO coated on multi-walled carbon nanotubes as a promising electrode for methanol electro-oxidation reaction in direct methanol fuel cell. *Solid State Sciences*, 97:106012, 2019.

[28] Dai, Z., Du, X., Wang, Y., Han, X. and Zhang, X. Promoting urea oxidation and water oxidation through interface construction on a CeO_2@$CoFe_2O_4$ heterostructure. *Dalton Transactions*, 50(35):12301-12307, 2021.

[29] Li, X. and Wang, J. One-dimensional and two-dimensional synergized nanostructures for high-performing energy storage and conversion. *InfoMat*, *2*(1):3-32, 2020.

[30] Baruah, B. and Kumar, A. PEDOT: PSS/MnO_2/rGO ternary nanocomposite based anode catalyst for enhanced electrocatalytic activity of methanol oxidation for direct methanol fuel cell. *Synthetic Metals*, 245:74-86, 2018.

[31] Baruah, B. and Kumar, A. rGO/PEDOT: PSS/$NiMn_2O_4$ Nanohybrid: An Inexpensive Anode Catalyst for Methanol and Ethylene Glycol Electro-Oxidation. *Journal of The Electrochemical Society*, 168(3):034510, 2021.

[32] Yang, R., Yuan, J., Yu, C., Yan, K., Fu, Y., Xie, H., Chen, J., Chu, P.K. and Wu, X. Efficient electromagnetic wave absorption by SiC/Ni/NiO/C nanocomposites. *Journal of Alloys and Compounds*, 816:152519, 2020.

[33] Latonen, R.M., Lönnqvist, J.E., Jalander, L., Kvarnström, C. and Ivaska, A. In situ spectroelectrochemical study on a copolymer made from the 2-biphenyl-3-octylthiophene monomer. *Electrochimica acta*, 51(7):1244-1254, 2006.

[34] Umeshbabu, E. and Rao, G.R. $NiCo_2O_4$ hexagonal nanoplates anchored on reduced graphene oxide sheets with enhanced electrocatalytic activity and stability for methanol and water oxidation. *Electrochimica Acta*, 213:17-729, 2016.

[35] Gajraj, V., Kumar, A., Ekta, D., Kaushik, R., Jose, D.A., Ghosh, A. and Mariappan, C.R. Multifunctionality exploration of $NiCo_2O_4$-rGO nanocomposites: photochemical water oxidation, methanol electro-oxidation and asymmetric supercapacitor applications. *Dalton Transactions*, 50(48):18001-18015, 2021.

[36] Ding, Y.L., Kopold, P., Hahn, K., van Aken, P.A., Maier, J. and Yu, Y. A lamellar hybrid assembled from metal disulfide nanowall arrays anchored on a carbon layer: in situ hybridization and improved sodium storage. *Advanced Materials*, 28(35):7774-7782, 2016.

[37] Wang, J., Teschner, D., Yao, Y., Huang, X., Willinger, M., Shao, L. and Schlögl, R. Fabrication of nanoscale NiO/Ni heterostructures as electrocatalysts for efficient methanol oxidation. *Journal of Materials Chemistry A*, 5(20):9946-9951, 2017.

[38] Wu, D., Zhang, W. and Cheng, D. Facile synthesis of Cu/NiCu electrocatalysts integrating alloy, core–shell, and one-dimensional structures for efficient methanol oxidation reaction. *ACS Applied Materials & Interfaces*, 9(23):19843-19851, 2017.

[39] Xiang, C., Zou, Y., Qiu, S., Sun, L., Xu, F. and Zhou, H. Bienzymatic glucose biosensor based on direct electrochemistry of cytochrome c on gold nanoparticles/polyaniline nanospheres composite. *Talanta*, 110:96-100, 2013.

[40] Pickup, P.G., Kuo, K.N. and Murray, R.W. Electrodeposition of metal particles and films by a reducing redox polymer. *Journal of the Electrochemical Society*, 130(11):2205, 1983.

[41] Yang, W., Gao, Z., Song, N., Zhang, Y., Yang, Y. and Wang, J. Synthesis of hollow polyaniline nano-capsules and their supercapacitor application. *Journal of Power Sources*, 272:915-921, 2014.

[42] Laviron, E.J.J. General expression of the linear potential sweep voltammogram in the case of diffusionless electrochemical systems. *Journal of Electroanalytical Chemistry and Interfacial Electrochemistry*, 101(1):19-28, 1979.

[43] Wang, T.J., Huang, H., Wu, X.R., Yao, H.C., Li, F.M., Chen, P., Jin, P.J., Deng, Z.W. and Chen, Y. Self-template synthesis of defect-rich NiO nanotubes as efficient electrocatalysts for methanol oxidation reaction. *Nanoscale*, 11(42):19783-19790, 2019.

[44] Fleischmann, M., Korinek, K. and Pletcher, D. The oxidation of organic compounds at a nickel anode in alkaline solution. *Journal of Electroanalytical Chemistry and Interfacial Electrochemistry*, 31(1):39-49, 1971.

[45] Fleischmann, M., Korinek, K. and Pletcher, D. The kinetics and mechanism of the oxidation of amines and alcohols at oxide-covered nickel, silver, copper, and cobalt electrodes. *Journal of the Chemical Society, Perkin Transactions* 2, (10):1396-1403, 1972.

[46] Al-Enizi, A.M., Ghanem, M.A., El-Zatahry, A.A. and Al-Deyab, S.S. Nickel oxide/nitrogen doped carbon nanofibers catalyst for methanol oxidation in alkaline media. *Electrochimica Acta*, 137:774-780, 2014.

[47] Taraszewska, J. and Rosłonek, G. Electrocatalytic oxidation of methanol on a glassy carbon electrode modified by nickel hydroxide formed by ex situ chemical precipitation. *Journal of Electroanalytical Chemistry*, 364(1-2):209-213, 1994.

[48] Cui, B., Wang, C., Huang, S., He, L., Zhang, S., Zhang, Z. and Du, M. Efficient multifunctional electrocatalyst based on 2D semiconductive bimetallic metal-organic framework toward non-Pt methanol oxidation and overall water splitting. *Journal of Colloid and Interface Science*, 578:10-23, 2020.

[49] Arunachalam, P., Ghanem, M.A., Al-Mayouf, A.M. and Al-shalwi, M. Enhanced electrocatalytic performance of mesoporous nickel-cobalt oxide electrode for methanol oxidation in alkaline solution. *Materials Letters*, 196:365-368, 2017.

[50] Singh, R.N. and Singh, A. Electrocatalytic activities of binary and ternary composite electrodes of Pd, nanocarbon and Ni for electro-oxidation of methanol in alkaline medium. *Journal of Solid State Electrochemistry*, 13(8):1259-1265, 2009.

[51] Žic, M. The influence of the PANI structure on the conductive mechanism and on the electrical equivalent circuit analysis. *Journal of Electroanalytical Chemistry,* 635(1):29-38, 2009.

[52] Jeon, J.S., Yu, I.K., Kim, W. and Choi, S.H. Electrocatalytic oxidation of methanol by a polymeric Ni complex-modified electrode prepared by a one-step cold-plasma process. *Frontiers in Chemistry,* 8:595616, 2020.